Journal of
Mechanics of
Materials and Structures

A DYNAMIC ELECTRO-THERMO-MECHANICAL MODEL OF DIELECTRIC BREAKDOWN IN SOLIDS USING PERIDYNAMICS

Raymond A. Wildman and George A. Gazonas

Volume 10, No. 5 December 2015

msp

JOURNAL OF MECHANICS OF MATERIALS AND STRUCTURES
Vol. 10, No. 5, 2015
dx.doi.org/10.2140/jomms.2015.10.613

A DYNAMIC ELECTRO-THERMO-MECHANICAL MODEL OF DIELECTRIC BREAKDOWN IN SOLIDS USING PERIDYNAMICS

RAYMOND A. WILDMAN AND GEORGE A. GAZONAS

The electro-thermo-mechanical breakdown of dielectric solids is modeled using peridynamics to describe the brittle fracture of a material under high electric fields. A coupled electrostatic, elastodynamic, thermodynamic model is used wherein electrostatic forces are computed and applied to the mechanical model and temperature effects are included. Fracture is simulated using peridynamics, a reformulation of elasticity that incorporates material failure. Coupling occurs between the electrostatic and mechanical forces and also the electrical material properties: specifically, the Lorentz and Kelvin forces are used to couple the electrostatic fields to the stress fields, conductivity is treated as nonlinear and a function of temperature, and mechanical damage is used to alter the permittivity. Results demonstrate that the method is capable of reproducing branching breakdown patterns seen in experiments using a deterministic method.

1. Introduction

Dielectric breakdown in a solid is a process involving the application of high voltage to a material, which leads to a rapid increase in the conductivity and temperature of that material, ultimately resulting in permanent material damage. In a solid material, an electromechanical breakdown process is accompanied by high temperatures, melting, vaporization, and ionization of the material, as well as physical fractures not necessarily associated with the rise in conductivity. Overall, dielectric breakdown represents a highly coupled multiphysics problem that can be challenging for numerical methods to capture.

The simulation of dielectric breakdown was first addressed with the dielectric breakdown model (DBM) or diffusion limited aggregation model [Niemeyer et al. 1984; Irurzun et al. 2002; Arshak et al. 2008]. The DBM is a stochastic method capable of reproducing the fractal patterns seen in the breakdown of various materials. Unfortunately, DBM is static and cannot reproduce breakdown velocity. Several other models are similar in nature in that they use networks of circuit components to model breakdown. These network models use fuse-like components that are destroyed when subjected to high fields [Joshi et al. 2002; Boksiner and Leath 2003; Quiña et al. 2008]. In addition to simulation methods, a simple relation between breakdown strength and a material's elastic properties can be derived, giving a rough estimate of electromechanical breakdown strength [Zebouchi and Malec 1998]. A coupled thermal/electrostatic model is given by [Noskov et al. 2001], which couples conductivity to temperature in a multiphysics model. A large field of study is focused on breakdown in thin films, in which a percolation model can be used to develop statistical characteristics [Lloyd et al. 2005; Nigam et al. 2009]. Parallels have been made between dielectric breakdown and the brittle fracture of materials under mechanical loading, leading to J-integral approaches [Beom and Kim 2008; Fan et al. 2009], a fracture energy-based approach [Schneider 2013], and a charge-free zone model [Zhang and Xie 2013]. Most

Keywords: dielectric breakdown, peridynamics, electromechanical, multiphysics.

recently, sophisticated, coupled methods have been proposed, which model the evolution of charge in gases [Chaudhury and Boeuf 2010] and liquids [Jadidian et al. 2013]. Finally, phase field modeling has been used to model the dynamic character of breakdown in a solid [Pitike and Hong 2014].

Many of the early methods discussed above are quasistatic in that they strictly dictate the breakdown velocity, though not the breakdown path. Most dynamic models are for thin films, which give accurate breakdown statistics for those geometries. The method presented here most closely resembles the coupled thermal/electrostatic model [Noskov et al. 2001], though here we extend that model through the addition of mechanical fracture. Similarly to that approach, breakdown is simulated as a change in conductivity and not using a specific breakdown field strength, such as that used in the phase field model [Pitike and Hong 2014]. The phase field approach assumes a breakdown field strength as a material property, and not as a measured quantity.

On the experimental side, dielectric breakdown can be difficult to study due to its short time scales and high energies. Despite this, several studies illustrate breakdown with high-speed photography [Yamada et al. 1990; Auckland et al. 1975; Budenstein 1980; Auckland et al. 1981]. Breakdown in solids has been studied in detail in single crystals in [Neusel et al. 2012]. In addition, the combined mechanical and electrical loading of glasses has been compared using fracture toughness, providing useful data for validating numerical schemes [Yan et al. 2010].

In the proposed approach, peridynamics will be used to simulate mechanical failure of a solid material. Peridynamics is a formulation of continuum mechanics that replaces the local divergence operators with nonlocal integral operators to facilitate fracture modeling [Silling 2000]. It has been shown to capture complex branching fracture patterns in brittle solids subjected to high mechanical loads [Ha and Bobaru 2010].

A method is proposed that uses a coupled peridynamic/finite difference method to model electromechanical breakdown in solids. The method will couple electrostatic potential, elastodynamic fields, temperature, and their constitutive models. Peridynamics is most readily discretized using a point-based scheme, compatible with finite difference methods [Wildman and Gazonas 2014], which will be used in the electrostatic simulation. In this model, thermal diffusion is ignored due to the short time scales and low thermal conductivities of the dielectrics considered, though temperature increase due to Joule heating is considered. Coupling occurs between the electrostatic forces and the elastic wave equation, the mechanical damage and the permittivity, the temperature and the conductivity, and the electric field and the conductivity [Flynn 1955; von Olshausen and Sachs 1981].

The remainder of the paper proceeds as follows: Section 2 discusses the coupled formulation including the relevant physics and discretization. Section 3 presents numerical results including homogeneous materials and materials with randomized conductivity of varying levels. Finally, Section 4 concludes the paper.

2. Formulation

The formulation of the coupled model is presented in this section. First, peridynamics is discussed in more detail, including its discretization and damage model. Next, the electrostatic solver is discussed, which uses a staggered grid to compute the electrostatic potential. The thermal model is then described, which only includes temperature increase due to Joule heating. Finally, the coupling of the various field equations and constitutive models is summarized.

2.1. ***Peridynamics.*** Peridynamics is a continuum model for brittle-elastic fracture [Silling 2000; Silling et al. 2007; Emmrich and Weckner 2006], which (in its original, bond-based form) replaces the divergence of the elastic stress tensor with an integral of a microforce function. It is characterized by a nonlocal interaction region, in that the force at a given point in space is influenced by the action at surrounding points at nonvanishing distances. The nonlocal region is governed by a specific size, or horizon, and it can be shown that for certain formulations, in the limit as this horizon approaches zero, elastodynamics is recovered [Silling and Lehoucq 2008; Lehoucq and Silling 2008]. For simplicity, a standard, bond-based peridynamics approach is used here, and summarized below.

A standard, body-force-free formulation of continuum elastodynamics (incorporating thermal expansion) can be stated as the partial differential equation

$$\rho \frac{\partial^2}{\partial t^2} \boldsymbol{u} = \nabla \cdot \bar{\boldsymbol{\tau}}, \tag{1}$$

where bold type with an overbar represents a second-rank tensor, the stress $\bar{\boldsymbol{\tau}}$ is given by

$$\bar{\boldsymbol{\tau}} = \bar{\bar{\boldsymbol{C}}} : \bar{\boldsymbol{\varepsilon}} = \bar{\bar{\boldsymbol{C}}} : \left[\tfrac{1}{2} (\nabla \boldsymbol{u} + \boldsymbol{u} \nabla) - \bar{\boldsymbol{\alpha}} \Delta T \right], \tag{2}$$

two overbars represent a fourth-rank tensor, ΔT is the temperature difference relative to ambient, $\bar{\boldsymbol{\alpha}}$ is the thermal expansion tensor, and $\bar{\bar{\boldsymbol{C}}}$ is a fourth-rank constitutive tensor. In 2D plane strain, the isotropic, linear elastic constitutive tensor is given in Voigt notation by

$$\bar{\bar{\boldsymbol{C}}} = \begin{bmatrix} 2\mu + \lambda & \lambda & 0 \\ \lambda & 2\mu + \lambda & 0 \\ 0 & 0 & \mu \end{bmatrix}, \tag{3}$$

where Lamé's parameters λ and μ are

$$\lambda = \frac{E\nu}{(1+\nu)(1-2\nu)} \tag{4}$$

and

$$\mu = \frac{E}{2(1+\nu)}, \tag{5}$$

and E is Young's modulus and ν is Poisson's ratio.

Peridynamics proposes to replace the divergence of the stress on the right-hand side of (1) with the integral-based internal force formulation

$$\rho \frac{\partial^2}{\partial t^2} \boldsymbol{u} = \int_{\mathcal{H}_r} \boldsymbol{f}(\boldsymbol{u}' - \boldsymbol{u}, \boldsymbol{r}' - \boldsymbol{r}, T)\, dV', \tag{6}$$

where $\mathcal{H}_r$ is the horizon at point $\boldsymbol{r}$ and is typically spherical with radius δ and the microforce function can be defined as

$$\boldsymbol{f}(\boldsymbol{\eta}, \boldsymbol{\xi}, T) = c[s(\boldsymbol{\eta}, \boldsymbol{\xi}) - \alpha \Delta T] \frac{\boldsymbol{\eta} + \boldsymbol{\xi}}{\|\boldsymbol{\eta} + \boldsymbol{\xi}\|}, \tag{7}$$

with bond stretch $s(\boldsymbol{\eta}, \boldsymbol{\xi})$ given as

$$s(\boldsymbol{\eta}, \boldsymbol{\xi}) = \frac{\|\boldsymbol{\eta} + \boldsymbol{\xi}\| - \|\boldsymbol{\xi}\|}{\|\boldsymbol{\xi}\|}, \tag{8}$$

c being a constitutive parameter, relatable to the elastic parameters as

$$c = \frac{6E}{\pi\delta^3(1-\nu)}. \tag{9}$$

Poisson's ratio is restricted to $\nu = \frac{1}{3}$ for plane stress and $\nu = \frac{1}{4}$ for plane strain [Ha and Bobaru 2010], and isotropic thermal expansion is modeled using the scalar thermal expansion coefficient α and temperature (relative to ambient) ΔT [Kilic and Madenci 2010; Oterkus and Madenci 2012; Oterkus et al. 2014].

Most importantly, peridynamics incorporates damage into its formulation by allowing for "bond-breaking" or the removal of points from horizons under high strain. The typical damage criterion is defined using the bond stretch s as

$$s - \alpha\Delta T > s_0, \tag{10}$$

where s_0 can be related to the fracture energy G_0 as [Ha and Bobaru 2010]

$$s_0 = \sqrt{\frac{4\pi G_0}{9E\delta}}. \tag{11}$$

If two bonds have a stretch that satisfies the inequality of (10), then those bonds are removed from each other's horizons. This approach is clearer in the discretized method, which will next be summarized.

Equation (6) is typically discretized in a pointwise fashion, wherein a domain is broken up into a regular grid and quadrature is performed with a simple midpoint rule. This approach will also be adopted here, though we will use exact quadrature weights at the edges of the horizon. In other words, where the horizon intersects with a rectangular cell, the exact area of that cell will be used, rather than the area of the entire cell as is sometimes used [Seleson 2014]. More specifically, (6) is discretized spatially as

$$\rho\frac{\partial^2}{\partial t^2}\boldsymbol{u}_{ij} = \sum_{m,n|\boldsymbol{r}_{mn}\in\mathcal{H}_{\boldsymbol{r}_{ij}}}^{N_{ij}} \boldsymbol{f}\left(\boldsymbol{\eta}_{ij,mn}, \boldsymbol{\xi}_{ij,mn}, \frac{\Delta T_{ij} + \Delta T_{mn}}{2}\right) V_{ij,mn}, \tag{12}$$

where $\boldsymbol{u}_{ij} = \boldsymbol{u}(\boldsymbol{r}_{ij})$, $\boldsymbol{\xi}_{ij,mn} = \boldsymbol{r}_{ij} - \boldsymbol{r}_{mn}$, $\boldsymbol{\eta}_{ij,mn} = \boldsymbol{u}_{ij} - \boldsymbol{u}_{mn}$, $V_{ij,mn}$ is the area (or volume in 3D) of the mn-th node in the horizon, $\mathcal{H}_{\boldsymbol{r}_{ij}}$, of node ij, and N_{ij} is the current number of nodes in the horizon of node ij. (In this section, the indices i, j, m, and n are used, though the mechanical variables will be solved on a staggered grid, offset by $\frac{1}{2}$ in both directions. For compactness, the factor of $\frac{1}{2}$ is dropped here. For the actual locations of all field variables, see Figure 1.) Temporal derivatives are discretized

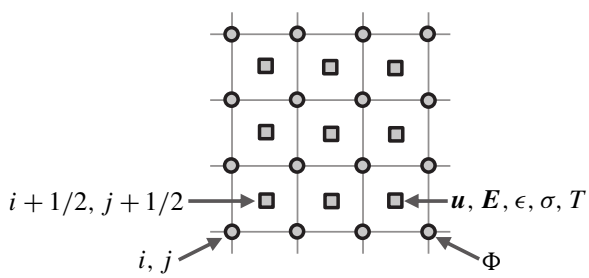

Figure 1. Staggered grid used for the numerical implementation, with variables labeled.

using a velocity-Verlet method, resulting in the update equations

$$\begin{aligned} \boldsymbol{v}^{k+1/2} &= \boldsymbol{v}^k + \frac{\Delta t}{2}\boldsymbol{a}^k, \\ \boldsymbol{u}^{k+1} &= \boldsymbol{u}^k + \Delta t\, \boldsymbol{v}^{k+1/2}, \\ \boldsymbol{a}^{k+1} &= \frac{\boldsymbol{F}_{\mathrm{PD}}}{\rho}, \\ \boldsymbol{v}^{k+1} &= \boldsymbol{v}^{k+1/2} + \frac{\Delta t}{2}\boldsymbol{a}^{k+1}, \end{aligned} \tag{13}$$

where $\boldsymbol{a} = \partial^2 \boldsymbol{u}/\partial t^2$ is the acceleration, $\boldsymbol{v} = \partial \boldsymbol{u}/\partial t$ is the velocity, $\boldsymbol{F}_{\mathrm{PD}}$ is the internal force given as the right-hand side of (12), and Δt is the time step size.

Finally, damage occurs when two nodes suffer a stretch exceeding the critical stretch (defined in (11)) and can be written in discretized form as

$$s_{ij,mn} = \frac{\|\boldsymbol{\eta}_{ij,mn} + \boldsymbol{\xi}_{ij,mn}\| - \|\boldsymbol{\xi}_{ij,mn}\|}{\|\boldsymbol{\xi}_{ij,mn}\|} - \alpha \frac{\Delta T_{ij} + \Delta T_{mn}}{2} > s_0. \tag{14}$$

In this case, any nodes satisfying the damage criterion will be removed from each other's horizons, thus decreasing N_{ij} for each. In other words, node mn will no longer contribute to the internal force of node ij in (12) (and vice versa). A damage parameter can then be defined as

$$d_{ij} = 1 - \frac{N_{ij}}{N_{ij}^{\mathrm{initial}}} \tag{15}$$

where $N_{ij}^{\mathrm{initial}}$ is the initial number of bonds in the horizon of node ij.

2.2. ***Electrostatic model.*** As peridynamics is most easily discretized with a particle method, a finite difference method is a natural choice for the electrostatic model. Here, the electrostatic forces will be computed beginning with the quasistatic model

$$\nabla \cdot (\sigma(T, \|\boldsymbol{E}\|)\nabla\Phi) + \frac{\partial}{\partial t}\nabla \cdot (\epsilon \nabla \Phi) = 0, \tag{16}$$

where $\sigma(T, |\boldsymbol{E}|)$ is the conductivity and is a nonlinear function of the electric field and temperature, ϵ is the permittivity, and Φ is the electrostatic potential [Koch and Weiland 2011]. Note that the electrical material properties are time-varying. As stated above, (16) is a quasistatic model and can be derived by starting from either Poisson's electrostatic equation or the conservation of charge. In both cases, current density is given by Ohm's law, which has the form

$$\boldsymbol{J} = \sigma \boldsymbol{E}, \tag{17}$$

where $\boldsymbol{J}$ is the current density. The quasistatic formulation used here is most appropriate for problems with finite conductivity, rather than infinite or zero as is assumed in many electrostatic problems. This formulation allows for a more accurate computation of charge and current flow, though no electromagnetic waves are generated.

In order to simplify the solution of (16), the conductivity will be linearized after temporal discretization. In other words, a Taylor series expansion will be used about the previous time step. For now, assume

that the conductivity is given by either

$$\sigma(T, \|\boldsymbol{E}\|) = \sigma_0 f_{\mathrm{m}}(T) e^{\gamma \|\boldsymbol{E}\|}, \tag{18}$$

or

$$\sigma(T, \|\boldsymbol{E}\|) = \sigma_0 e^{\gamma \|\boldsymbol{E}\|} + f_{\mathrm{a}}(T), \tag{19}$$

where σ_0 is the conductivity at low temperature and field, $f_{\mathrm{m}}(T)$ and $f_{\mathrm{a}}(T)$ are some functional dependence on the temperature T, and γ is a parameter of the model. In addition, we assume coupling between material damage d (defined in (15)) and permittivity, modeling the formation of voids. Here, we use a linear relationship between damage and permittivity:

$$\epsilon_{ij} = \epsilon_0[\epsilon_r(1 - d_{ij}) + d_{ij}], \tag{20}$$

corresponding to a permittivity of $\epsilon_r\epsilon_0$ when $d_{ij} = 0$ and ϵ_0 when $d_{ij} = 1$, where ϵ_0 is the permittivity of free space.

This model is spatially discretized using a staggered grid for the material properties and a weak form given by

$$\oint_{\partial\Omega} \sigma \nabla\Phi \cdot \hat{\boldsymbol{n}}\, d\ell + \frac{\partial}{\partial t} \oint_{\partial\Omega} \epsilon \nabla\Phi \cdot \hat{\boldsymbol{n}}\, d\ell = 0, \tag{21}$$

where the material properties are assumed to be constant through the region Ω enclosed by the contour $\partial\Omega$ with unit normal $\hat{\boldsymbol{n}}$. A region Ω_{ij} is then rectangular with side lengths Δx and Δy, centered on the point $\boldsymbol{r}_{ij}$. The electrostatic potential is then solved at each point $\boldsymbol{r}_{ij}$ and denoted as Φ_{ij}. Applying a finite difference approximation to $\nabla\Phi$, along with the assumption of constant material properties in each Ω_{ij} and equal grid spacing along both x and y (i.e., $\Delta x = \Delta y$) gives the discretization

$$\nabla \cdot (a\nabla\Phi) \approx -A_0\Phi_{ij} + A_1\Phi_{i+1,j} + A_2\Phi_{i,j+1} + A_3\Phi_{i-1,j} + A_4\Phi_{i,j-1}, \tag{22}$$

where

$$\begin{aligned}
A_0 &= a_{i+1/2,j+1/2} + a_{i+1/2,j-1/2} + a_{i-1/2,j+1/2} + a_{i-1/2,j-1/2},\\
A_1 &= \tfrac{1}{2}(a_{i+1/2,j+1/2} + a_{i+1/2,j-1/2}),\\
A_2 &= \tfrac{1}{2}(a_{i-1/2,j+1/2} + a_{i+1/2,j+1/2}),\\
A_3 &= \tfrac{1}{2}(a_{i-1/2,j-1/2} + a_{i-1/2,j+1/2}),\\
A_4 &= \tfrac{1}{2}(a_{i+1/2,j-1/2} + a_{i-1/2,j-1/2})
\end{aligned} \tag{23}$$

and a is an inhomogeneous material property.

In addition to the above discretization, we require a finite difference approximation incorporating an anisotropic material due to the linearization of the conductivity (discussed below). Generically, for anisotropic materials, the first term of (21) becomes

$$\oint_{\partial\Omega} (\bar{\boldsymbol{B}} \nabla\Phi) \cdot \hat{\boldsymbol{n}}\, d\ell, \tag{24}$$

where $\bar{\boldsymbol{B}}$ is a second-rank tensor representing a generic anisotropic material property. The numerical formulation for an isotropic material can then be extended by following the same assumptions, in particular that the materials and derivative approximations are constant along each part of the contour integral.

Following this procedure leads to

$$\nabla \cdot (\bar{\boldsymbol{B}} \nabla \Phi) \approx -B_0 \Phi_{ij} + B_1 \Phi_{i+1,j} + B_2 \Phi_{i,j+1} + B_3 \Phi_{i-1,j} + B_4 \Phi_{i,j-1}, \tag{25}$$

where

$$B_0 = \tfrac{1}{2}(b^{xx}_{i+1/2,j+1/2} + b^{xx}_{i+1/2,j-1/2} + b^{xx}_{i-1/2,j+1/2} + b^{xx}_{i-1/2,j-1/2}) + \tfrac{1}{2}(b^{yy}_{i+1/2,j+1/2} + b^{yy}_{i+1/2,j-1/2} + b^{yy}_{i-1/2,j+1/2} + b^{yy}_{i-1/2,j-1/2}), \tag{26}$$

$$B_1 = \tfrac{1}{2}(b^{xx}_{i+1/2,j+1/2} + b^{xx}_{i+1/2,j-1/2}) + \tfrac{1}{4}(b^{yx}_{i+1/2,j+1/2} + b^{yx}_{i-1/2,j+1/2}) - \tfrac{1}{4}(b^{yx}_{i-1/2,j-1/2} + b^{yx}_{i+1/2,j-1/2}), \tag{27}$$

with the remaining terms B_2, B_3, and B_4 being derived similarly, and the b^{xx}, b^{xy}, b^{yx}, and b^{yy} are the corresponding components of $\bar{\boldsymbol{B}}$.

The spatially discretized equation can then be written as

$$D_\sigma \Phi + \frac{\partial}{\partial t} D_\epsilon \Phi = 0, \tag{28}$$

where D_a is the discretized operator defined above and D_σ is a nonlinear function of the potential. Because the permittivity is time-varying in this model, the above is rewritten

$$D_\sigma \Phi + D_{\partial\epsilon/\partial t} \Phi + D_\epsilon \frac{\partial}{\partial t} \Phi = 0. \tag{29}$$

An implicit backward Euler approximation can then be applied to the temporal derivatives, giving

$$(\Delta t D_{\sigma^k} + 2 D_{\epsilon^k} - D_{\epsilon^{k-1}}) \Phi^k = D_{\epsilon^k} \Phi^{k-1}, \tag{30}$$

where Δt is the time step size. Now, the nonlinearity in the conductivity can be linearized by expanding the conductivity (given in (18) or (19)) times the electric field in a Taylor series about the field at the previous time step, $\boldsymbol{E}^{k-1}$:

$$\sigma(T^k, \|\boldsymbol{E}^k\|)\boldsymbol{E}^k \approx \sigma_0 f_{\mathrm{m}}(T^k) e^{\gamma \|\boldsymbol{E}^{k-1}\|} \left[\boldsymbol{E}^k + \gamma \frac{\boldsymbol{E}^{k-1} \otimes \boldsymbol{E}^{k-1}}{\|\boldsymbol{E}^{k-1}\|} (\boldsymbol{E}^k - \boldsymbol{E}^{k-1}) \right], \tag{31}$$

where $\otimes$ denotes a tensor outer product so that the second term behaves as an anisotropic material, necessitating the use of (25)–(27). (Using the version of the conductivity given in (19) follows similarly.) Noting that $\boldsymbol{E} = -\nabla\Phi$ and using the notation of (30), we find

$$(\Delta t D_{\sigma_1^k} + \Delta t D_{\sigma_2^k} + 2 D_{\epsilon^k} - D_{\epsilon^{k-1}}) \Phi^k = (D_{\epsilon^k} + \Delta t D_{\sigma_2^k}) \Phi^{k-1}, \tag{32}$$

where the conductivity terms $D_{\sigma_1^k}$ and $D_{\sigma_2^k}$ are the discretizations of the first and second terms of the linearization in (31) as given by (22)–(23) and (25)–(27), respectively. After appropriate boundary conditions are applied, (32) can be solved at each time step for the electrostatic potential.

Next, forces can be computed from the electrostatic potential by computing the electric field, $\boldsymbol{E}$, charge density, $q = \nabla \cdot (\epsilon \boldsymbol{E})$, and polarization vector $\boldsymbol{P}$ and applying the Lorentz force

$$\boldsymbol{F}_{\mathrm{L}} = q \boldsymbol{E} \tag{33}$$

and the Kelvin polarization force

$$\boldsymbol{F}_{\mathrm{K}} = \boldsymbol{P} \cdot \nabla \boldsymbol{E}, \tag{34}$$

where the polarization vector $\boldsymbol{P}$ is given by

$$\boldsymbol{P} = (\epsilon - \epsilon_0)\boldsymbol{E}, \tag{35}$$

and ϵ is the permittivity of the dielectric [Lewis 1998]. The electric field $\boldsymbol{E}$ is computed from a finite difference approximation of $\boldsymbol{E} = -\nabla\Phi$, and the charge density q is computed from a finite difference approximation of Gauss's law.

Another advantage of the staggered-grid approach adopted above is that we actually require the electric field, not just the electrostatic potential. The electric field can be computed on the material grid as

$$\begin{aligned} \hat{\boldsymbol{x}} \cdot \boldsymbol{E}_{i+1/2,\, j+1/2} &\approx -\frac{\Phi_{i+1,j+1} - \Phi_{i,j} - \Phi_{i,j+1} + \Phi_{i+1,j}}{2\Delta x}, \\ \hat{\boldsymbol{y}} \cdot \boldsymbol{E}_{i+1/2,\, j+1/2} &\approx -\frac{\Phi_{i+1,j+1} - \Phi_{i,j} + \Phi_{i,j+1} - \Phi_{i+1,j}}{2\Delta y}. \end{aligned} \tag{36}$$

The advantage here is that the potential Φ was computed on a grid offset from the grid used for the material properties and hence the peridynamic simulation. The forces needed for the peridynamic simulation must be computed by finite difference of the potential, so we can again take advantage of the offset grid and use a central difference.

These electrostatic forces are then coupled to the mechanical simulation with the equation of motion

$$\rho \frac{\partial^2}{\partial t^2}\boldsymbol{u} = \boldsymbol{F}_{\mathrm{PD}} + \boldsymbol{F}_{\mathrm{L}} + \boldsymbol{F}_{\mathrm{K}}, \tag{37}$$

where $\boldsymbol{F}_{\mathrm{PD}}$ represents the mechanical forces found on the right-hand side of (12).

A simplifying assumption used here is that the mechanical displacement does not couple to the electrostatic simulation. In other words, relative motion implied by any nonzero displacement is ignored in the computation of the electrostatic potential.

2.3. ***Thermal model.*** Typically, the heat equation for a coupled thermomechanical problem will include terms depending on mechanical heating, diffusion, and any heat sources. Here, the thermodynamics of the model is dominated by Joule heating, so mechanical heating is ignored. Also, due to the short time scales and low thermal conductivities of most dielectric materials, thermal diffusion can be ignored. Joule heating is then defined as

$$Q = \boldsymbol{J} \cdot \boldsymbol{E}, \tag{38}$$

where Q is the power generated per unit volume due to current density $\boldsymbol{J}$. The conduction current density is then given by (17), giving

$$Q = \sigma \|\boldsymbol{E}\|^2. \tag{39}$$

The temperature at a point in space can be computed by summing the power at each point via

$$\frac{\partial}{\partial t} T = \frac{1}{c_{\mathrm{p}}\rho} Q, \tag{40}$$

where c_p is the specific heat capacity of the material at constant pressure and ρ is again the mass density. An explicit forward Euler discretization of the above gives

$$T^{k+1} = T^k + \frac{\Delta t}{c_\mathrm{p}\rho} Q. \tag{41}$$

The temperature is also used to alter material properties, specifically conductivity. Typically, an Arrhenius-type relation is used for temperature-conductivity coupling [Boggs and Kuang 1998; Noskov et al. 2001], which has a temperature dependency of $\exp(-aT^{-1})$. This type of temperature dependence can be included as an additive term to the conductivity as

$$f_\mathrm{a}(T_{ij}) = \begin{cases} \sigma_1 e^{-\beta_1 T_{ij}^{-1}}, & T_{ij} < T_\mathrm{v}, \\ \sigma_2 e^{-\beta_2 T_{ij}^{-1}}, & T_{ij} \geq T_\mathrm{v}, \end{cases} \tag{42}$$

where two phases can be included depending on the temperature. The parameters σ_1, σ_2, β_1, β_2, and T_v are given.

In addition, a basic exponential-type multiplicative model can be stated as [Nyberg et al. 1975]

$$f_\mathrm{m}(T_{ij}) = \begin{cases} 1, & T_{ij} < T_\mathrm{m}, \\ e^{\beta(T_{ij} - T_\mathrm{m})}, & T_\mathrm{m} \leq T_{ij} < T_\mathrm{v}, \\ f_\mathrm{max}, & T_{ij} \geq T_\mathrm{v}, \end{cases} \tag{43}$$

where the coefficient β is given by

$$\beta = \frac{\log(f_\mathrm{max})}{T_\mathrm{v} - T_\mathrm{m}}. \tag{44}$$

In addition, if the temperature exceeds T_v, the conductivity is fixed at a maximum value, which will be $\sigma = 10^6\,\mathrm{S\,m^{-1}}$ throughout. In this model, the temperatures T_m and T_v may then refer to phase changes at which it may be expected that temperature influences the conductivity of the material. Temperature T_m is used to indicate the point at which the temperature begins to affect conductivity, and temperature T_v is the point at which temperature no longer influences conductivity.

Several coupled effects are ignored in the current model. Specifically, neglected but expected first- or second-order effects include the mechanical material properties dependence on temperature and the energy required to complete phase changes. Here, mechanical material properties (including the damage criterion) are not dependent on temperature while typically a material will soften as it approaches its melting point. In this model, temperatures may span all states of matter for a given material, so accurate material temperature-dependent models may be difficult to find in the literature. Also, phase changes and the energy required to complete a phase change are also ignored. A phase change from solid to liquid will of course change the governing equation of motion, though in this model, typically if the temperature rises above a certain point, enough damage has already been accumulated so that the material is not effectively behaving as a solid. Also, equations of state are not used to model gas pressure exerted on the damaged material. These effects will be considered in a future implementation. Other effects that may not be as significant include the dependence of the electrostatic potential on deformation, thermal diffusion, and the heat generated by mechanical deformation.

2.4. ***Algorithm summary.*** The algorithm sequence can be summarized as follows.

(1) Specify any initial electrical material properties given by the problem geometry, and compute initial potential.

(2) Update the displacement and velocity based on acceleration using (13).

(3) Update the temperature using (41).

(4) Compute the damage due to bond-breakage using condition (14) and the internal forces $\boldsymbol{F}_{\mathrm{PD}}$.

(5) Update the permittivity based on the damage using (20).

(6) Update the conductivity based on the electric field and temperature using (31).

(7) Compute the electrostatic potential (Φ) from (16), with specified initial and boundary conditions.

(8) Compute the electrostatic forces from the potential ($\boldsymbol{F}_{\mathrm{L}}$ and $\boldsymbol{F}_{\mathrm{K}}$) with (33) and (34).

(9) Update the velocity and acceleration using the all forces $\boldsymbol{F}_{\mathrm{PD}}$, $\boldsymbol{F}_{\mathrm{L}}$, and $\boldsymbol{F}_{\mathrm{K}}$.

(10) Repeat starting at Item (2).

In addition, Figure 2 illustrates the time-stepping process: arrows indicate the dependence of variables at various points in the algorithm. The algorithm progresses to the right (increasing k) and upward on the diagram as indicated by the arrows.

In both simulations (electrostatic and peridynamic), the spatial grid and time step size are the same, though the electrostatic potential is solved on an offset grid (see Figure 1). In this case, the time step size is governed by the requirements of the peridynamic simulation, which has a Courant-like stability condition [Silling and Askari 2005], and the accuracy of the linearization of the conductivity as given in (31). The spatial grid size is determined by the input geometry, as typically sharp features are required to produce a high electric field necessary for breakdown. Though this approach is deterministic, some random noise may be added to the electrical material properties to generate stochastic breakdown patterns.

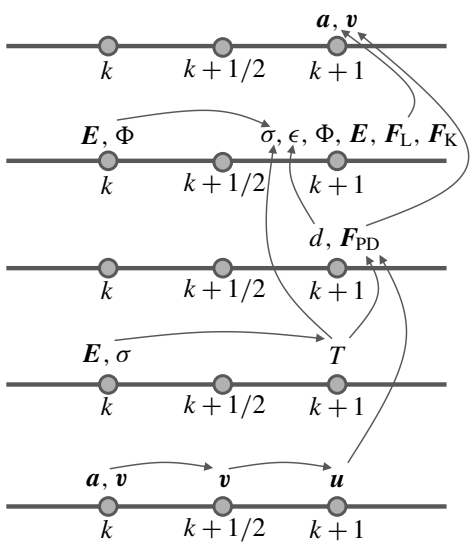

Figure 2. Schematic diagram of the time-stepping sequence.

Mechanical:	$\rho = 2400\ \mathrm{kg\,m^{-3}}$; $E = 72\ \mathrm{GPa}$; $\delta = 0.15\ \mathrm{mm}$; $G_0 = 5\ \mathrm{J\,m^{-2}}$
Electrical:	$\epsilon_0 = 8.85 \times 10^{-12}\ \mathrm{F\,m^{-1}}$; $\epsilon_r = 20$; $\sigma_0 = 10^{-19}\ \mathrm{S\,m^{-1}}$
Thermal:	$c_\mathrm{p} = 800\ \mathrm{J\,kg^{-1}\,K^{-1}}$; $T_\mathrm{m} = 500\ \mathrm{K}$; $T_\mathrm{v} = 1000\ \mathrm{K}$
Coupled:	$\alpha = 9 \times 10^{-6}\ \mathrm{K^{-1}}$; $f_\mathrm{max} = 100$; $\gamma = 5 \times 10^{-8}\ \mathrm{m\,V^{-1}}$

Table 1. Physical constants.

Field equations. The relevant field equations are summarized as three unknowns ($\boldsymbol{u}$, Φ, and T) and the three equations

$$\rho \frac{\partial^2}{\partial t^2}\boldsymbol{u} = \boldsymbol{F}_\mathrm{PD} + \boldsymbol{F}_\mathrm{L} + \boldsymbol{F}_\mathrm{K}, \tag{45}$$

$$\nabla \cdot (\sigma(T, \|\boldsymbol{E}\|)\nabla\Phi) + \frac{\partial}{\partial t}\nabla \cdot (\epsilon \nabla\Phi) = 0, \tag{46}$$

$$\frac{\partial}{\partial t}T = \frac{1}{c_\mathrm{p}\rho}Q. \tag{47}$$

Each equation is discretized spatially using either finite differences or a grid-based mesh-free approach. Temporal discretizations are also finite difference-based, though the electrostatic equation uses backward Euler, the peridynamic equation uses velocity Verlet, and the thermodynamic equation uses forward Euler.

Constitutive models. The coupled constitutive models (using the multiplicative form of the temperature-conductivity coupling) are summarized as

$$\epsilon_{ij} = \epsilon_0[\epsilon_r(1 - d_{ij}) + d_{ij}], \tag{48}$$

$$\sigma_{ij}^k = \sigma_0 f_\mathrm{m}(T_{ij}^k) e^{\gamma \|\boldsymbol{E}_{ij}^{k-1}\|}\left[\boldsymbol{E}_{ij}^k + \gamma \frac{\boldsymbol{E}_{ij}^{k-1} \otimes \boldsymbol{E}_{ij}^{k-1}}{\|\boldsymbol{E}_{ij}^{k-1}\|}(\boldsymbol{E}_{ij}^k - \boldsymbol{E}_{ij}^{k-1})\right], \tag{49}$$

$$f_\mathrm{m}(T_{ij}) = \begin{cases} 1, & T_{ij} < T_\mathrm{m}, \\ e^{\beta(T_{ij} - T_\mathrm{m})}, & T_\mathrm{m} \le T_{ij} < T_\mathrm{v}, \\ f_\mathrm{max}, & T_{ij} \ge T_\mathrm{v}. \end{cases} \tag{50}$$

In total, the permittivity depends on the damage (which depends on the mechanical deformation) and the conductivity depends on the temperature and electric field. The thermal properties (thermal conductivity and specific heat) are not coupled in this model, and neither are the mechanical properties.

Constants. Finally, the physical constants encompass the typical constants for the electrical, thermal, and mechanical properties, as well coupling constants needed in the constitutive models listed above. Typical values of these constants are given in Table 1 and will be used in Section 3 unless specified otherwise. The mechanical constants, thermal expansion coefficient, and heat capacity used here resemble a soda-lime glass, while the electrical and other coupling coefficients are chosen arbitrarily. Some constants, such as the coupling coefficient γ, can be difficult to find in the literature for many materials, so reasonable values are assumed. In addition, the effect of the temperature-conductivity coupling coefficient f_max is studied below. Future work will include validation of the model with experiments.

3. Numerical results

Several numerical results will be presented in this section. Throughout, a point-plane geometry will be analyzed using the material properties listed in Table 1. In addition to the homogeneous material case, randomized conductivity will be demonstrated. Discretization refinement will also be explored. Finally, the effect of the temperature-conductivity coupling coefficients will be studied.

In each example, the voltage of the ground plane is fixed at 0, the point probe is held at a voltage described below, and (for simplicity) the remaining sides are treated as homogeneous Neumann boundary conditions. In each case, the voltage given ($V_{\max}$) is the maximum voltage following an exponential ramp, according to

$$\Phi_{\text{probe}}(t) = V_{\max}(1 - e^{-t/\tau}), \tag{51}$$

where the time constant is $\tau = 0.3\,\mu$s in each case.

3.1. ***Uniform material properties: weak temperature dependence.*** A point-plane-type geometry was simulated first with uniform material properties, wherein a point probe of length 2.5 mm and width 150 μm was suspended above a ground plane separated by a distance of 7.5 mm. The simulation region was 10 mm $\times$ 10 mm. The material properties listed in Table 1 were used along with a spatial discretization of $\Delta x = \Delta y = 50\,\mu$m and a temporal discretization of 1 ns. The simulation was run for 5000 time steps (5 μs) for two different maximum voltages. First, a maximum voltage of 3 MV was used with the mechanical fracture damage shown in Figure 3, left. The electric field at the final time is shown in Figure 3, right, in units of V m^{-1}.

A maximum voltage of 4 MV was simulated next, using a spatial discretization of $\Delta x = \Delta y = 40\,\mu$m, peridynamic horizon of $\delta = 0.12$ mm, and the same temporal discretization and material properties as above. Figure 4, left, shows the damage after 5 μs, Figure 4, right, shows the magnitude of the electric field, and Figure 5 shows the conductivity on a logarithmic scale. Clearly, the increased maximum voltage leads to higher damage in the material. Also note that, due to the weak dependence of the conductivity on temperature, the fractures observed are not associated with high conductivity. This is in contrast to typical dielectric breakdown models in which all breakdown or material damage is associated with high conductivity. Stronger dependence of conductivity on temperature is explored in a subsequent subsection.

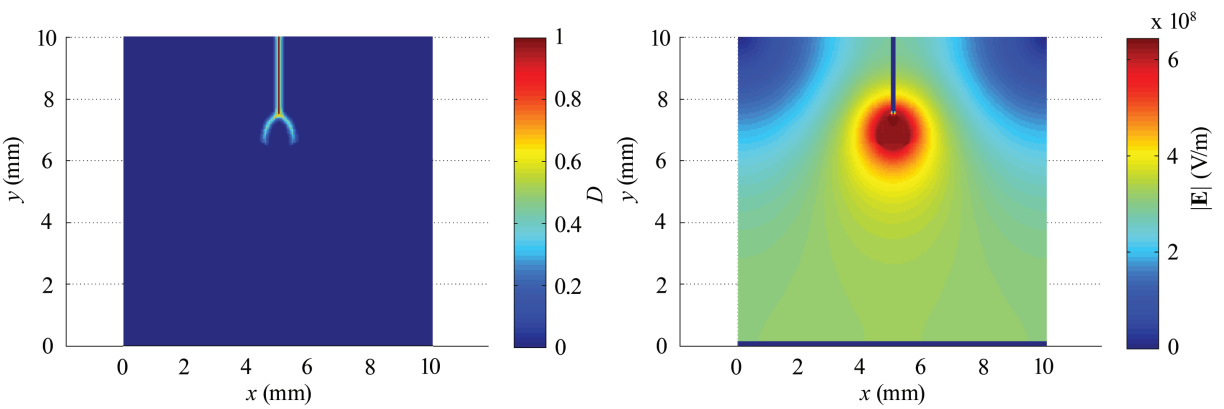

Figure 3. Mechanical damage including point electrode (left) and electric field (right) after 5 μs with $V_{\max} = 3$ MV.

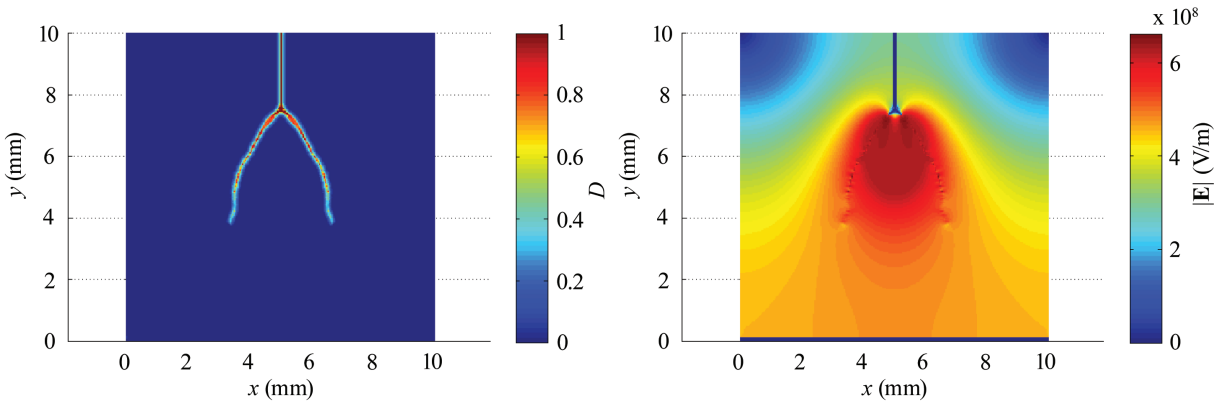

Figure 4. Mechanical damage including point electrode (left) and electric field (right) after 5 μs with $V_{\max} = 4$ MV.

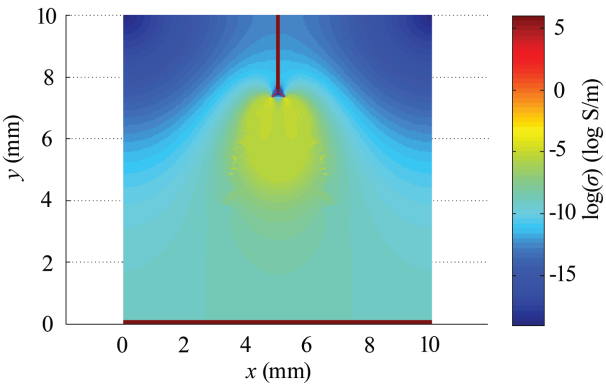

Figure 5. Conductivity after 5 μs with $V_{\max} = 4$ MV.

3.2. ***Randomized conductivity: weak temperature dependence.*** A random, background conductivity will be added following a Gaussian distribution. The distribution will set the exponent of the conductivity so that the actual conductivity is exponentially related to the random distribution. More specifically, the randomized background conductivity is set as

$$\sigma_0(\boldsymbol{r}_{ij}) = \sigma_m + 10^{R(\sigma_m,\omega)}, \tag{52}$$

where $\sigma_m = 10^{-19}$ is the base material's conductivity and $R(\mu, \omega)$ is a random variable from Gaussian distribution with mean μ and standard deviation ω. The standard deviation will be varied to alter the background conductivity.

First, a maximum voltage of 3 MV was simulated (using the same discretization as the 3 MV example above) with a standard deviation of $\omega = 6$ used to alter the background conductivity. The results after 5 μs are shown in Figure 6 (damage and conductivity). By comparison with Figure 3, left, it can be seen that the damage pattern is similar in extent, though its path is altered by the randomized conductivity.

Next, a maximum voltage of 4 MV was simulated again using the same discretization and material properties as the 4 MV above. The background conductivity was again randomized using a standard

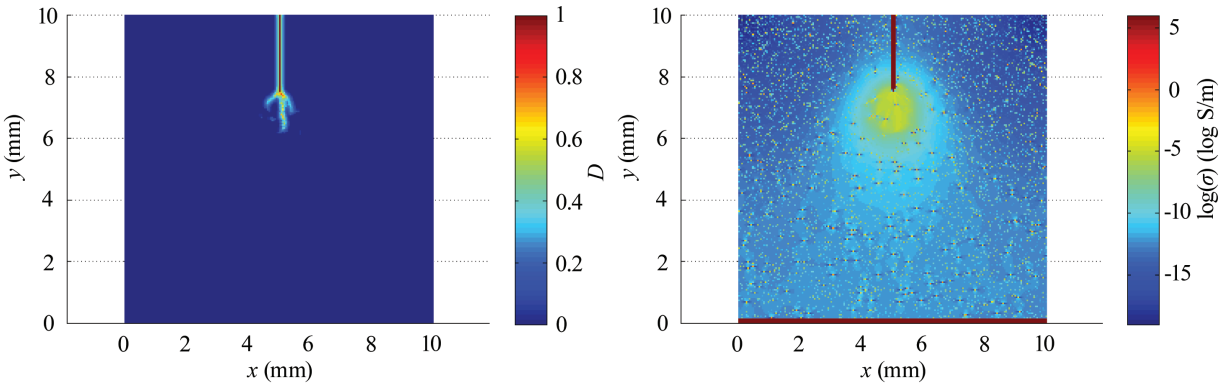

Figure 6. Mechanical damage including point electrode (left) and conductivity on a log scale (right) after 5 μs with $V_{\max} = 3$ MV with randomized background conductivity.

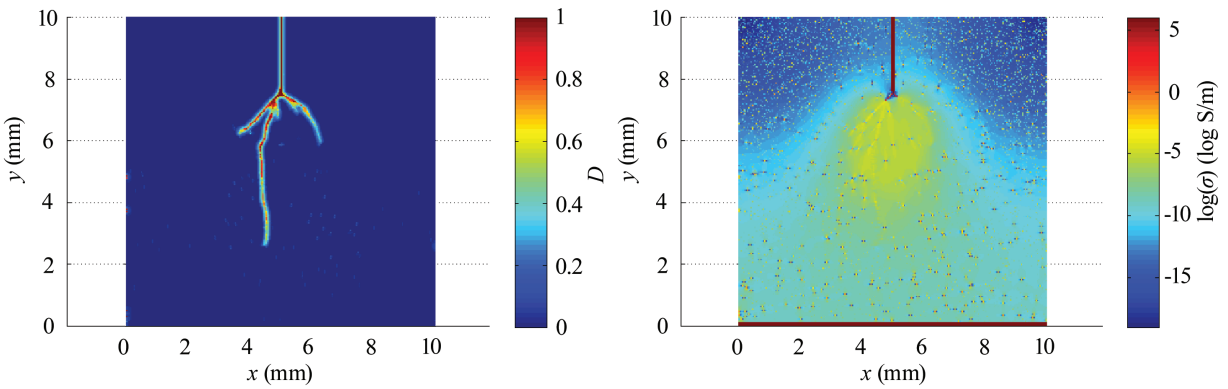

Figure 7. Mechanical damage including point electrode (left) and conductivity on a log scale (right) after 5 μs with $V_{\max} = 4$ MV with randomized background conductivity.

deviation of $\omega = 6$, though the actual distribution of conductivity is not the same as the above example. In other words, the conductivity was generated using a different seed for the random number generator. Figure 7 shows the damage after 5 μs (left) and the conductivity on a logarithmic scale (right).

3.3. ***Discretization refinement.*** The above test with a maximum voltage of 4 MV was repeated, though now with a time step size of $\Delta t = 0.5$ ns. The resulting damage is shown in Figure 8, left. As can be seen by comparing with Figure 4, left, the damage pattern is stable between the two time step sizes.

Next, the breakdown simulation was run with a spatial discretization of $\Delta x = \Delta y = 33.33\,\mu$m, a peridynamic horizon of $\delta = 0.1$ mm, and a time step size of $\Delta t = 1$ ns. In this case, the width of the point probe had to be reduced to 100 μm to conform to the computational grid. Nevertheless, the results show a stable fracture pattern (Figure 8, right) compared with the coarse discretization.

3.4. ***Strong temperature dependence.*** Due to positive feedback, increasing the temperature-conductivity coupling coefficient ($f_{\max}$ or β) leads to much higher temperatures than those seen in the previous examples. The model is not formulated to couple temperature to all relevant material properties (e.g.,

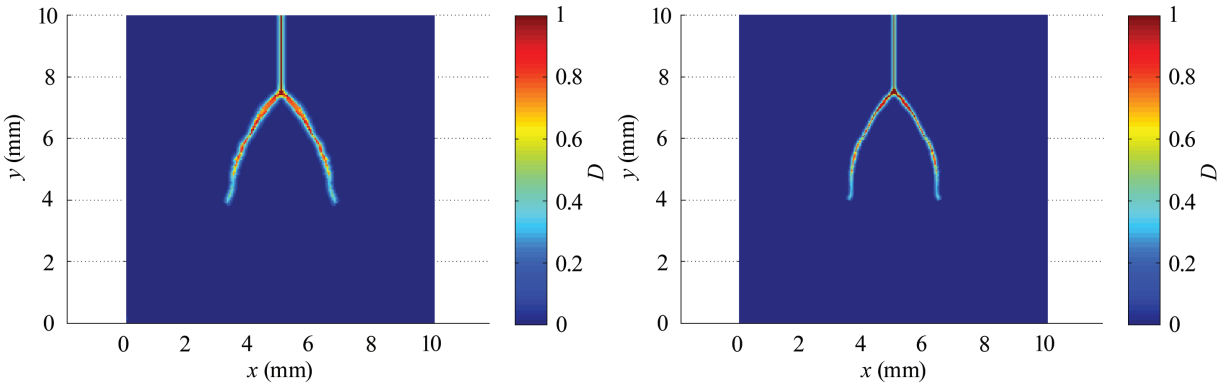

Figure 8. Mechanical damage including point electrode after 5 μs with $V_{\max} = 4$ MV using a time step size of $\Delta t = 0.5$ ns (left) and using a spatial step size of $\Delta x = \Delta y = 33.33$ μm (right).

mechanical properties), so a first approach is to limit the maximum Joule heating power allowed in the simulation. In this section, a maximum heating power of $Q = 10^{16}$ W is used. An immediate effect seen if higher temperatures are allowed is that the thermal expansion can lead to rapid degradation of the material and instability in the simulation.

In this example, the temperature-conductivity coupling coefficient was raised to $f_{\max} = 10^6$. Uniform material properties were used with the coarse discretization in both space and time of the 4 MV example above. A maximum voltage of 4 MV was simulated, giving the damage seen in Figure 9. With the increased coupling coefficient, the damage pattern has changed and now has an additional branch originating at the ground plane.

3.5. ***Additive temperature-conductivity model.*** Finally, the additive form (see (42)) of the temperature-conductivity coupling is tested. The parameters used are transition temperature $T_{\mathrm{v}} = 1000$ K, base conductivities of $\sigma_1 = 10^4\,\mathrm{S\,m^{-1}}$ and $\sigma_2 = 3 \times 10^4\,\mathrm{S\,m^{-1}}$, and exponents of $\beta_1 = 1.2 \times 10^4\,\mathrm{K^{-1}}$ and

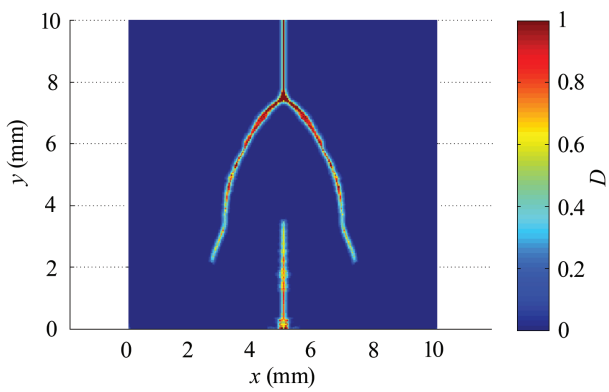

Figure 9. Mechanical damage including point electrode after 5 μs with $V_{\max} = 4$ MV using a temperature-conductivity coupling coefficient of $f_{\max} = 10^6$.

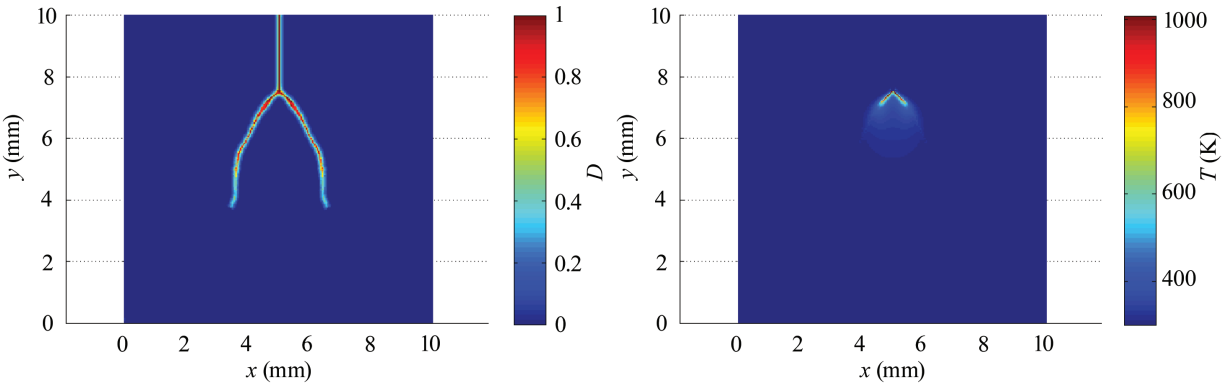

Figure 10. Mechanical damage including point electrode (left) and temperature distribution (right) after 5 μs with $V_{\max} = 4$ MV using the additive temperature-conductivity coupling model.

$\beta_2 = 1.2 \times 10^3\ \mathrm{K}^{-1}$. The simulation was run with both a maximum voltage of 3 MV and 4 MV. With a maximum voltage of 3 MV and 4 MV, the resulting damage was similar to that given above for the weak temperature dependence. The damage after 5 μs for a maximum voltage of 4 MV is shown in Figure 10, left. The temperature after 5 μs is shown in Figure 10, right, illustrating that, while there is mechanical fracture in the material, a highly conductive region has not propagated completely through the material.

4. Conclusions

A coupled electrostatic, thermodynamic, elastodynamic model of dielectric breakdown in solids was presented. The method uses a finite difference solver to compute the electrostatic potential due to an applied voltage. The Lorentz and Kelvin forces couple the electric field to the mechanical forces, thus generating stress in the solid. Peridynamics is used to then simulate the mechanical fracture of the material due to high strains. The electrical permittivity is coupled to the damage, and a nonlinear conductivity is used to model the effects of high electric fields. Finally, temperature is considered in the model using Joule heating as the heat source, and thermal expansion and temperature effects on the electrical conductivity are considered. Results show mechanical fracture patterns consistent with those seen in brittle solids undergoing dielectric breakdown. In addition, discretization refinement was performed and shows that the proposed method generates stable fracture patterns. Several additions to the model are possible, for example, coupling of temperature to mechanical material properties, deformation to electrostatic potential, and more realistic phase changes.

References

[Arshak et al. 2008] K. Arshak, I. Guiney, and E. Forde, "Material dependent dielectric breakdown model", *Comp. Mater. Sci* **42**:3 (2008), 483–488.

[Auckland et al. 1975] D. W. Auckland, A. B. Borishade, and N. Gravill, "A self triggered high speed camera for the photography of prebreakdown luminescence in solid dielectrics", *J. Phys. E Sci. Instrum.* **8**:10 (1975), 847–849.

[Auckland et al. 1981] D. W. Auckland, R. Cooper, and J. Sanghera, "Photographic investigation of formative stage of electric breakdown in diverging fields", *IEE Proc. A* **128**:3 (1981), 209–214.

[Beom and Kim 2008] H. G. Beom and Y. H. Kim, "Application of J integral to breakdown analysis of a dielectric material", *Int. J. Solids Struct.* **45**:24 (2008), 6045–6055.

[Boggs and Kuang 1998] S. Boggs and J. Kuang, "High field effects in solid dielectrics", *IEEE Electr. Insul. M.* **14**:6 (1998), 5–12.

[Boksiner and Leath 2003] J. Boksiner and P. L. Leath, "Dynamics of dielectric breakdown paths", *Phys. Rev. E* **67**:6 (2003), 066610.

[Budenstein 1980] P. P. Budenstein, "On the mechanism of dielectric breakdown of solids", *IEEE T. Electr. Insul.* **15**:3 (1980), 225–240.

[Chaudhury and Boeuf 2010] B. Chaudhury and J.-P. Boeuf, "Computational studies of filamentary pattern formation in a high power microwave breakdown generated air plasma", *IEEE T. Plasma Sci.* **38**:9 (2010), 2281–2288.

[Emmrich and Weckner 2006] E. Emmrich and O. Weckner, "The peridynamic model in non-local elasticity theory", *P. Appl. Math. Mech.* **6**:1 (2006), 155–156.

[Fan et al. 2009] C.-Y. Fan, M.-H. Zhao, and Y.-H. Zhou, "Numerical solution of polarization saturation/dielectric breakdown model in 2D finite piezoelectric media", *J. Mech. Phys. Solids* **57**:9 (2009), 1527–1544.

[Flynn 1955] P. T. G. Flynn, "Field-dependent conductivity in non-uniform fields and its relation to electrical breakdown", *P. IEE C Monogr.* **102**:2 (1955), 264–269.

[Ha and Bobaru 2010] Y. D. Ha and F. Bobaru, "Studies of dynamic crack propagation and crack branching with peridynamics", *Int. J. Fracture* **162**:1–2 (2010), 229–244.

[Irurzun et al. 2002] I. M. Irurzun, P. Bergero, V. Mola, M. C. Cordero, J. L. Vicente, and E. E. Mola, "Dielectric breakdown in solids modeled by DBM and DLA", *Chaos Soliton. Fract.* **13**:6 (2002), 1333–1343.

[Jadidian et al. 2013] J. Jadidian, M. Zahn, N. Lavesson, O. Widlund, and K. Borg, "Stochastic and deterministic causes of streamer branching in liquid dielectrics", *J. Appl. Phys.* **114**:6 (2013), 063301.

[Joshi et al. 2002] R. P. Joshi, J. Qian, and K. H. Schoenbach, "Electrical network-based time-dependent model of electrical breakdown in water", *J. Appl. Phys.* **92**:10 (2002), 6245–6251.

[Kilic and Madenci 2010] B. Kilic and E. Madenci, "Peridynamic theory for thermomechanical analysis", *IEEE T. Adv. Packaging* **33**:1 (2010), 97–105.

[Koch and Weiland 2011] S. Koch and T. Weiland, "Different types of quasistationary formulations for time domain simulations", *Radio Sci.* **46**:5 (2011), 1–7.

[Lehoucq and Silling 2008] R. B. Lehoucq and S. A. Silling, "Force flux and the peridynamic stress tensor", *J. Mech. Phys. Solids* **56**:4 (2008), 1566–1577.

[Lewis 1998] T. J. Lewis, "A new model for the primary process of electrical breakdown in liquids", *IEEE T. Dielect. El. In.* **5**:3 (1998), 306–315.

[Lloyd et al. 2005] J. R. Lloyd, E. Liniger, and T. M. Shaw, "Simple model for time-dependent dielectric breakdown in inter- and intralevel low-k dielectrics", *J. Appl. Phys.* **98**:8 (2005), 084109.

[Neusel et al. 2012] C. Neusel, H. Jelitto, D. Schmidt, R. Janssen, F. Felten, and G. A. Schneider, "Dielectric breakdown of alumina single crystals", *J. Eur. Ceram. Soc.* **32**:5 (2012), 1053–1057.

[Niemeyer et al. 1984] L. Niemeyer, L. Pietronero, and H. J. Wiesmann, "Fractal dimension of dielectric breakdown", *Phys. Rev. Lett.* **52**:12 (1984), 1033–1036.

[Nigam et al. 2009] T. Nigam, A. Kerber, and P. Peumans, "Accurate model for time-dependent dielectric breakdown of high-k metal gate stacks", pp. 523–530 in *2009 IEEE International Reliability Physics Symposium* (Montréal, 2009), Inst. El. Electr. Eng., Piscataway, NJ, 2009.

[Noskov et al. 2001] M. Noskov, V. Lopatin, A. Cheglokov, and A. Shapovalov, "Computer simulation of discharge channel propagation in solid dielectric", pp. 465–468 in *Proceedings of the 2001 IEEE 7th International Conference on Solid Dielectrics* (Eindhoven, Netherlands, 2001), Inst. El. Electr. Eng., Piscataway, NJ, 2001.

[Nyberg et al. 1975] B. R. Nyberg, K. Herstad, and K. Bjorlow-Larsen, "Numerical methods for calculation of electrical stresses in HVDC cables with special application to the Skagerrak cable", *IEEE T. Power. Ap. Syst.* **94**:2 (1975), 491–497.

[von Olshausen and Sachs 1981] R. von Olshausen and G. Sachs, "AC loss and DC conduction mechanisms in polyethylene under high electric fields", *IEE Proc. A* **128**:3 (1981), 183–192.

[Oterkus and Madenci 2012] E. Oterkus and E. Madenci, "Peridynamic analysis of fiber-reinforced composite materials", *J. Mech. Mater. Struct.* **7**:1 (2012), 45–84.

[Oterkus et al. 2014] S. Oterkus, E. Madenci, and A. Agwai, "Fully coupled peridynamic thermomechanics", *J. Mech. Phys. Solids* **64** (2014), 1–23.

[Pitike and Hong 2014] K. C. Pitike and W. Hong, "Phase-field model for dielectric breakdown in solids", *J. Appl. Phys.* **115**:4 (2014), 044101.

[Quiña et al. 2008] P. L. D. Quiña, L. Herrera, I. M. Irurzun, and E. E. Mola, "A capacitive model for dielectric breakdown in polymer materials", *Comp. Mater. Sci* **44**:2 (2008), 330–338.

[Schneider 2013] G. A. Schneider, "A Griffith type energy release rate model for dielectric breakdown under space charge limited conductivity", *J. Mech. Phys. Solids* **61**:1 (2013), 78–90.

[Seleson 2014] P. Seleson, "Improved one-point quadrature algorithms for two-dimensional peridynamic models based on analytical calculations", *Comput. Methods Appl. Mech. Engrg.* **282** (2014), 184–217.

[Silling 2000] S. A. Silling, "Reformulation of elasticity theory for discontinuities and long-range forces", *J. Mech. Phys. Solids* **48**:1 (2000), 175–209.

[Silling and Askari 2005] S. A. Silling and E. Askari, "A meshfree method based on the peridynamic model of solid mechanics", *Comput. Struct.* **83**:17–18 (2005), 1526–1535.

[Silling and Lehoucq 2008] S. A. Silling and R. B. Lehoucq, "Convergence of peridynamics to classical elasticity theory", *J. Elasticity* **93**:1 (2008), 13–37.

[Silling et al. 2007] S. A. Silling, M. Epton, O. Weckner, J. Xu, and E. Askari, "Peridynamic states and constitutive modeling", *J. Elasticity* **88**:2 (2007), 151–184.

[Wildman and Gazonas 2014] R. A. Wildman and G. A. Gazonas, "A finite difference-augmented peridynamics method for reducing wave dispersion", *Int. J. Fracture* **190**:1–2 (2014), 39–52.

[Yamada et al. 1990] H. Yamada, T. Sato, and T. Fujiwara, "High-speed photography of prebreakdown phenomena in dielectric liquids under highly non-uniform field conditions", *J. Phys. D Appl. Phys.* **23**:12 (1990), 1715–1722.

[Yan et al. 2010] D.-J. Yan, H.-Y. Huang, C.-W. Cheung, and T.-Y. Zhang, "Fracture criterion for conductive cracks in soda-lime glass under combined mechanical and electrical loading", *Int. J. Fracture* **164**:2 (2010), 185–199.

[Zebouchi and Malec 1998] N. Zebouchi and D. Malec, "Combination of thermal and electromechanical breakdown mechanisms to analyze the dielectric breakdown in polyethylene terephthalate", *J. Appl. Phys.* **83**:11 (1998), 6190–6192.

[Zhang and Xie 2013] T.-Y. Zhang and T. Xie, "The charge-free zone model for electrically conductive cracks in dielectric and piezoelectric ceramics", *Acta Mech.* **224**:6 (2013), 1159–1168.

Received 15 Apr 2015. Revised 29 Sep 2015. Accepted 19 Oct 2015.

RAYMOND A. WILDMAN: raymond.a.wildman.civ@mail.mil
Weapons and Materials Research Directorate, U.S. Army Research Laboratory, Aberdeen Proving Ground, MD 21005, United States

GEORGE A. GAZONAS: george.a.gazonas.civ@mail.mil
Weapons and Materials Research Directorate, U.S. Army Research Laboratory, Aberdeen Proving Ground, MD 21005, United States

JOURNAL OF MECHANICS OF MATERIALS AND STRUCTURES

msp.org/jomms

Founded by Charles R. Steele and Marie-Louise Steele

Cover photo: Wikimedia Commons

See msp.org/jomms for submission guidelines.

JoMMS (ISSN 1559-3959) at Mathematical Sciences Publishers, 798 Evans Hall #6840, c/o University of California, Berkeley, CA 94720-3840, is published in 10 issues a year. The subscription price for 2015 is US $565/year for the electronic version, and $725/year (+$60, if shipping outside the US) for print and electronic. Subscriptions, requests for back issues, and changes of address should be sent to MSP.

JoMMS peer-review and production is managed by EditFLOW® from Mathematical Sciences Publishers.

PUBLISHED BY

mathematical sciences publishers

nonprofit scientific publishing

http://msp.org/

Journal of Mechanics of Materials and Structures

Volume 10, No. 5 December 2015

Special issue on

Peridynamic Theory